






Impedance Rhythms in Human Limbic System

 Filip Mivalt,^{1,2,3*}  Vaclav Kremen,^{1,4*} Vladimir Sladky,^{1,3,5} Jie Cui,¹ Nicholas M. Gregg,¹ Irena Balzekas,^{1,6} Victoria Marks,^{1,6} Erik K. St Louis,⁷  Paul Croarkin,⁸ Brian Nils Lundstrom,¹ Noelle Nelson,¹ Jiwon Kim,¹  Dora Hermes,⁶ Steven Messina,⁹ Samuel Worrell,¹ Thomas Richner,¹ Benjamin H. Brinkmann,^{1,6} Timothy Denison,¹⁰ Kai J. Miller,¹¹ Jamie Van Gompel,¹¹ Matthew Stead,¹ and  Gregory A. Worrell^{1,6}

¹Bioelectronics Neurophysiology and Engineering Laboratory, Department of Neurology, Mayo Clinic, Rochester, Minnesota 55905, ²Department of Biomedical Engineering, Faculty of Electrical Engineering and Communication, Brno University of Technology, 61600 Brno, Czech Republic, ³International Clinical Research Center, St. Anne's University Hospital, 60200 Brno, Czech Republic, ⁴Czech Institute of Informatics, Robotics, and Cybernetics, Czech Technical University, 16000 Prague, Czech Republic, ⁵Faculty of Biomedical Engineering, Czech Technical University, 16000 Prague, Czech Republic, ⁶Department of Physiology and Biomedical Engineering, Mayo Clinic, Rochester, Minnesota 55905, ⁷Center for Sleep Medicine, Departments of Neurology and Medicine, Divisions of Sleep Neurology and Pulmonary and Critical Care Medicine, Mayo Clinic, Rochester, Minnesota 55905, ⁸Departments of Psychiatry and Psychology and, ⁹Department of Radiology, Mayo Clinic Rochester, Minnesota 55905, ¹⁰Department of Engineering Science, Medical Research Council Brain Network Dynamics Unit, University of Oxford, Oxford OX3 7DQ, United Kingdom, and ¹¹Department of Neurologic Surgery, Mayo Clinic, Rochester, Minnesota 55905

The impedance is a fundamental electrical property of brain tissue, playing a crucial role in shaping the characteristics of local field potentials, the extent of ephaptic coupling, and the volume of tissue activated by externally applied electrical brain stimulation. We tracked brain impedance, sleep–wake behavioral state, and epileptiform activity in five people with epilepsy living in their natural environment using an investigational device. The study identified impedance oscillations that span hours to weeks in the amygdala, hippocampus, and anterior nucleus thalamus. The impedance in these limbic brain regions exhibit multiscale cycles with ultradian (~1.5–1.7 h), circadian (~21.6–26.4 h), and infradian (~20–33 d) periods. The ultradian and circadian period cycles are driven by sleep–wake state transitions between wakefulness, nonrapid eye movement (NREM) sleep, and rapid eye movement (REM) sleep. Limbic brain tissue impedance reaches a minimum value in NREM sleep, intermediate values in REM sleep, and rises through the day during wakefulness, reaching a maximum in the early evening before sleep onset. Infradian (~20–33 d) impedance cycles were not associated with a distinct behavioral correlate. Brain tissue impedance is known to strongly depend on the extracellular space (ECS) volume, and the findings reported here are consistent with sleep–wake–dependent ECS volume changes recently observed in the rodent cortex related to the brain glymphatic system. We hypothesize that human limbic brain ECS changes during sleep–wake state transitions underlie the observed multiscale impedance cycles. Impedance is a simple electrophysiological biomarker that could prove useful for tracking ECS dynamics in human health, disease, and therapy.

Key words: brain impedance; circadian rhythm; extracellular space; implantable neural stimulators; long-term data; sleep

Received Feb. 7, 2023; revised Aug. 9, 2023; accepted Aug. 14, 2023.

Author contributions: V.K., J.K., K.J.M., M.S., T.R., and G.A.W. designed research; F.M., V.K., V.S., J.C., N.M.G., I.B., V.M., E.K.S., P.C., B.N.L., N.N., J.K., S.M., B.H.B., T.D., K.J.M., J.V.G., and G.A.W. performed research; F.M., V.K., V.S., J.C., N.N., D.H., B.H.B., T.R., and G.A.W. contributed unpublished reagents/analytic tools; F.M., V.K., V.S., J.C., N.M.G., I.B., V.M., E.K.S., P.C., B.N.L., N.N., J.K., D.H., B.H.B., T.D., K.J.M., J.V.G., T.R., and G.A.W. analyzed data; F.M., V.S., N.M.G., S.W., T.D., K.J.M., J.V.G., and G.A.W. wrote the paper.

This work was supported by National Institutes of Health–National Institute of Neurological Disorders and Stroke Grants UH2&3 NS095495, R01 NS112144, R01 NS092882, R01 MH122258, and U24 NS113637; Defense Advanced Research Projects Agency Grant HR0011-20-2-0028; Mayo Clinic; and Research Center for Informatics, Czech Technical University. V.K. was partially supported by Czech Technical University. The devices were donated by Medtronic as part of the National Institutes of Health Brain Initiative. We thank Karla Crockett, Cindy Nelson, and Starr Guzman from Mayo Clinic for patient coordination; Abbey Becker, Dave Linde, and Scott Stanslaski from Medtronic for providing engineering support for the RC+S devices; Medtronic for the donation of the Summit RC+S devices; and OpenMind for providing community expertise and resources (<https://openmind-consortium.github.io/>).

*F.M. and V.K. contributed equally to this work.

Unrelated to this research, G.A.W., B.H.B., J.V.G., and B.N.L. are named inventors for intellectual property developed at Mayo Clinic and licensed to Cadence Neuroscience. G.A.W. has licensed intellectual property developed at Mayo Clinic to NeuroOne. B.N.L., G.A.W., and N.M.G. are investigators for the Medtronic Deep Brain Stimulation Therapy for the Epilepsy Post-Approval Study. V.K. consults for Certicon. I.B. has received compensation from an internship with Cadence Neuroscience for work unrelated to the current work. Mayo Clinic has received research support and consulting fees on behalf of G.A.W., B.N.L., and B.H.B. from Cadence Neuroscience, UNEEG Medical, NeuroOne, Epiminder, Medtronic, and Philips Neuro. P.C. has received research grant support from Neuronetics, NeoSync, and Pfizer; grant in kind (equipment support) from Assurex, MagVenture, and Neuronetics; and served as a consultant for Engrail Therapeutics, Myriad Neuroscience, Procter & Gamble, and Sunovion. T.D. is a consultant for Synchro, is on the advisory board of Cortec Neuro, is a shareholder collaborator of Bioinduction, and a shareholder director of Amber Therapeutics. T.D. has patents in the field of impedance measurement instrumentation and its application for epilepsy seizure prediction. All the other authors declare no competing financial interests.

Correspondence should be addressed to Gregory A. Worrell at worrell.gregory@mayo.edu.
<https://doi.org/10.1523/JNEUROSCI.0241-23.2023>

Copyright © 2023 the authors

Significance Statement

The electrical impedance in limbic brain structures (amygdala, hippocampus, anterior nucleus thalamus) is shown to exhibit oscillations over multiple timescales. We observe that impedance oscillations with ultradian and circadian periodicities are associated with transitions between wakefulness, NREM, and REM sleep states. There are also impedance oscillations spanning multiple weeks that do not have a clear behavioral correlate and whose origin remains unclear. These multiscale impedance oscillations will have an impact on extracellular ionic currents that give rise to local field potentials, ephaptic coupling, and the tissue activated by electrical brain stimulation. The approach for measuring tissue impedance using perturbational electrical currents is an established engineering technique that may be useful for tracking ECS volume.

Introduction

Electrical impedance is an extrinsic tissue property that characterizes the frequency-dependent resistance to endogenously generated ionic currents (Logothetis et al., 2007) and externally applied electrical stimulation currents (Butson et al., 2007) in the brain. The impedance influences the spatiotemporal dynamics of extracellular ionic currents that give rise to local field potentials (LFPs; Logothetis et al., 2007; Buzsáki et al., 2012) and determines the range of ephaptic coupling (Anastassiou et al., 2011; Jefferys et al., 2012; Qiu et al., 2015) and the volume of tissue activated by electrical brain stimulation (EBS; Butson et al., 2007). The voltage generated in response to an externally applied current can be used to probe and track brain impedance, and at the scale of clinical EBS electrodes ($\sim\text{mm}^2$), the impedance depends on the electrode–tissue interface and ionic current conductance through the intracellular, vascular, and extracellular space (ECS) brain compartments (Ranck, 1970). The impedance of rodent (Ranck, 1966, 1970), nonhuman primate (Logothetis et al., 2007), and human (Koessler et al., 2017) brain tissue is known to be primarily resistive over the frequency range of physiologic LFP (Miceli et al., 2017) and is strongly dependent on the ECS volume fraction (Ranck, 1966; Nicholson and Hrabětová, 2017). The interstitial conductive-fluid filled ECS creates a complex electrical network of ionic current flow that is increasingly recognized for its role in sleep-dependent brain health, such as clearing neurotoxic metabolites and pathologic proteins associated with neurodegenerative disorders (Xie et al., 2013; Holth et al., 2019; Hablitz and Nedergaard, 2021).

Brain tissue impedance is commonly treated as a constant, and the temporal dynamics of impedance have received relatively little attention despite being an integral factor in brain electrophysiology. Prior studies have investigated the role of impedance in LFP propagation (Logothetis et al., 2007; Miceli et al., 2017) and the volume of tissue activated by EBS (Butson et al., 2007). In nonhuman primates (Lempka et al., 2009) and in humans undergoing chronic therapeutic EBS for epilepsy (Sillay et al., 2013), the impedance was reported to initially increase after electrode implantation but then over a few weeks reach a constant stable value. In patients undergoing short-term invasive EEG monitoring for focal epilepsy, lower impedance in the tissue generating seizures was also reported (Koessler et al., 2017). These studies in humans, however, were limited to sparse temporal sampling of impedance and are inadequate for investigating impedance temporal dynamics and the effect of the sleep–wake behavioral state.

Two-photon imaging and real-time iontophoretic tetramethylammonium diffusion studies (Nicholson, 1993) of rodent cortex were previously used to show that the ECS volume is $\sim 60\%$ larger under anesthesia and in slow-wave, nonrapid eye

movement (NREM) sleep compared with wakefulness (Xie et al., 2013). The ECS volume expansion in slow-wave NREM sleep is associated with increased ECS interstitial and CSF exchange and β -amyloid clearance (Xie et al., 2013). Similar investigations have not been possible in humans, and whether similar behavioral state-dependent ECS dynamics are present in humans remains unclear. Notably, increased ECS volume in NREM compared with rapid-eye-movement (REM) sleep was previously proposed as the mechanism underlying electrical impedance increases observed during NREM to REM transitions in rodent brain (Ranck, 1966, 1970). We hypothesized that if sleep–wake transitions drive changes in human brain ECS volume, similar to the rodent glymphatic system, this would manifest as impedance cycles with lower impedance in NREM sleep, given the increased ECS volume compared with wakefulness and REM sleep. To test this hypothesis, we used a novel investigational implantable neural sensing and stimulation device (Kremen et al., 2018; Stanslaski et al., 2018; Giron et al., 2021) to continuously track impedance, sleep–wake behavioral state (Mivalt et al., 2022), and epileptiform activity (Sladky et al., 2022) in anterior nucleus of thalamus (ANT), amygdala (AMG), and hippocampus (HPC) over several months in five people with drug-resistant mesial temporal lobe epilepsy living in their natural home environment (Fig. 1).

Materials and Methods

Protocol and experimental design

People with drug-resistant mesial temporal lobe epilepsy were investigated under Federal Drug Administration (FDA) Investigational Device Exemption G180224 and Mayo Clinic Institutional Review Board (IRB) 18–005483 Human Safety and Feasibility Study of Neurophysiologically Based Brain State Tracking and Modulation in Focal Epilepsy (<https://clinicaltrials.gov/ct2/show/NCT03946618>). The final reporting of the primary outcome measures for this study will be completed in 2024 and will (1) report adverse events experienced during the investigational Medtronic Summit RC+S device trial, (2) demonstrate the feasibility of 24/7 continuous LFP monitoring, and (3) demonstrate continuous long-term tracking of seizures, interictal epileptiform spikes (IES), mood, anxiety, and memory.

Human subjects

Seven subjects with drug resistant mesial temporal lobe epilepsy were identified for the study and provided written consent in accordance with Mayo Clinic IRB and FDA requirements. Five subjects ultimately met the full inclusion criteria with adequate numbers of baseline seizures and were implanted with the investigational neural sensing and stimulation device (Medtronic RC+S Summit). The demographics and clinical information of the five subjects implanted with the Medtronic RC+S are provided in Table 1.

Experimental design and statistical analyses

The epilepsy patient assistant (EPA) is a custom software application running on a handheld computer enabling bidirectional

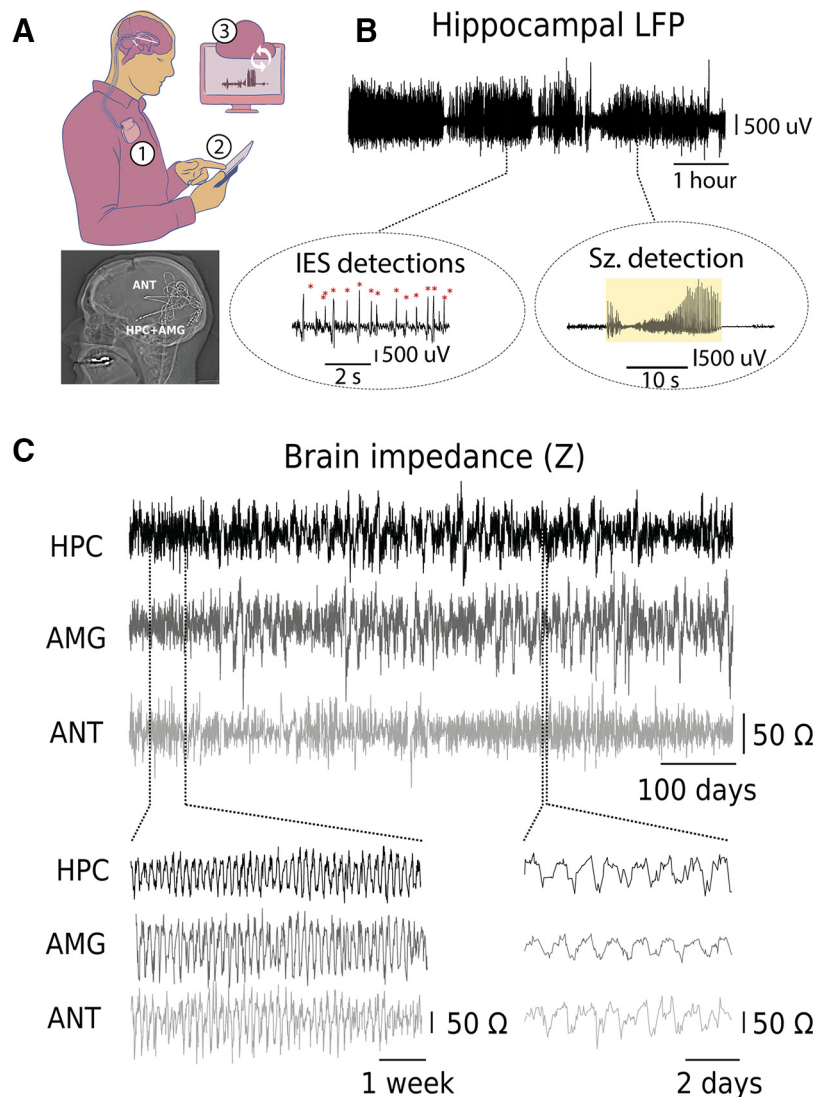


Figure 1. Monitoring human brain electrophysiology and behavior. Continuous wireless streaming of LFPs and brain impedance (Z) was used to investigate and track human brain electrophysiology in five ambulatory subjects with mesial temporal lobe epilepsy living in their natural home environment. **A**, The EPA system enables synchronized bidirectional communications between patient, implantable neural sensing, and stimulation devices (investigational Medtronic RC+S Summit), and local (tablet and smartphone) and distributed cloud computing infrastructure. The system consists of (1) RC+S implanted in a surgically created subclavicular pocket and connected to four electrode leads implanted in bilateral ANT and AMG-HPC. Bottom, Lateral x-ray of the bilateral ANT (3387-leads) and bilateral AMG-HPC (3391-lead) targets. The 3391-lead has four contacts (surface area, 11.97 mm²) spanning 24.5 mm. The contacts are 3.0 mm long and separated by 4.0 mm. The 3387-lead has four contacts (contact surface area, 5.985 mm²) spanning 10.5 mm. The individual contacts are 1.5 mm long and separated by 1.5 mm. (2) The EPA custom software application running on a tablet computer provides local computing and bidirectional connectivity between devices. (3) Cloud data and the analytics platform. **B**, Continuous streaming of brain LFP enables monitoring of epileptiform activity [IES and seizure (Sz)] and Z. Bottom Circles show automated IES and seizure detections. **C**, Representative raw impedance time series from HPC, AMG, and ANT recorded over multiple months from the subject living in natural home environment. Bottom, Expanded time scales of average Z (z score with 2 h median filter) showing 24 h cycles over multiple days and weeks.

communication between the implanted device, wearables, and cloud computing resources. The EPA features include automated algorithms for continuous LFP data acquisition, electrical stimulation, impedance testing, LFP analysis and an interface for collecting patient interactions (Kremen et al., 2018; Pal Attia et al., 2021).

The investigational Medtronic RC+S is an investigational implantable device with bidirectional wireless communication capability, programmable 16-channel electrical stimulation, two-point impedance measurements, and continuous four-channel (selected bipolar pairs) wireless LFP streaming to a handheld computer and cloud environment (Kremen et al., 2018; Stanslaski et al., 2018; Gilron et al., 2021).

For lead and electrode contact localization (Fig. 1A), five subjects (M1, 2, 3, 4, 5) had four leads stereotactically implanted into bilateral ANT and bilateral AMG-HPC. All five subjects had Medtronic 3387

implanted in the ANT. All subjects had AMG-HPC sites implanted with Medtronic 3391 leads, except the left HPC of M2. Subject M2 had previously undergone a left anterior temporal lobectomy leaving only a residual left HPC tail that was implanted with a Medtronic 3387-lead. Subject M5 does not have a right AMG electrode contact because of a technical problem at the time of surgery. The 3391-lead tail could not be fully seated into the lead extension connector, leaving only three of the four contacts recording. For each patient, the four leads (16 total electrode contacts) implanted were localized with postoperative CT scan coregistered to the preoperative MRI for anatomic localization using previously described pipelines (Hermes et al., 2010; Horn et al., 2019). The CT scan and electrode contact positions were coregistered to a T1-weighted anatomic MRI scan using coregistration in SPM12 software (<https://fil.ion.ucl.ac.uk/spm/>; Penny et al., 2011). FreeSurfer (<http://surfer.nmr.mgh.harvard.edu/>) software was used to segment the T1-weighted MRI and the electrodes labeled according to the

Table 1. Patient demographics and clinical information

Subject	Age, hand (L/R), (M/F), age onset (yrs), DRE (yrs)	Risk Factor, medical, surgical	Seizures FAS, FIAS, FTBC	ASM Current/previous	EEG	MRI
M1	57 yrs, R, F Onset, 9 y.o. DRE, 36 yrs	RF, TBI Medical, anxiety and depression Surgical, none	FAS, FIAS, rare FTBC	1. GBP, CZP 2. LEV, OXC PHT, CBZ	1. B. IES, TL Szs. 2. B. HPC IES, Szs L > R. IES, Szs. IES, L > R ($p < 0.001$) Szs, L > R ($p < 0.001$)	MRI, normal PET, N/A SPECT, N/A
M2	20 yrs R, F Onset, 7 y.o. DRE, 3 yrs	RF, none Medical, anxiety, depression, and Type 1 diabetes. Surgical, L. TL resection at 9 y.o.	FAS, FIAS, rare FTBC	1. LCM, CLZ, 2. LEV, PHT, CBZ, OXC	1. B. IES, TL Sz. 2. B. HPC IES, Sz. L > R. IES, Sz. IES, L > R ($p < 0.001$) Sz. L > R ($p < 0.001$)	MRI, L. TL resection. PET, N/A SPECT, N/A
M3	41 yrs R, F Onset, 31 y.o. DRE, 10 yrs	RF, none Medical, anxiety, depression, GAD-65 positive serum/CSF Surgical, VNS at 36 y.o.	FAS, FIAS, rare FTBC	1. CLZ, LEV, 2. CNB 3. LZP, CBZ, 4. PHT, TPX, 5. LCM, CBD	1. B. IES, TL Szs. 2. B. HPC IES, Szs L > R. IES IES, L > R ($p < 0.001$) Szs, L > R ($p < 0.8561$)	MRI, normal PET, N/A SPECT, N/A
M4	35 yrs R, F Onset, 4 y.o. DRE, 7 yrs	RF, none Medical, anxiety, depression, GAD-65 positive serum/CSF Surgical, none	FAS, FIAS, rare FTBC	1. OXC, LEV 2. LCM, CBZ, PHT, LGT	1. B. IES, TL Szs. 2. B. HPC IES, Szs L > R. IES, Szs. IES, L > R ($p < 0.001$) Szs, L > R ($p < 0.001$)	MRI, normal PET, N/A SPECT, N/A
M5	31 yrs R, M Onset, 22 y.o. DRE, 5 yrs	RF: TBI and family hx. Medical, anxiety, depression Surgical, none	FAS, FIAS, rare FTBC	1. LCM, VPA 2. LEV, LGT, PHT, CBZ	1. B. IES, TL Szs. 2. B. HPC IES, Szs L > R. IES, Szs. IES, L > R ($p < 0.001$) Szs, L > R ($p < 0.001$) IES, L > R ($p < 0.001$)	MRI, L. HPC atrophy, incr. T2 signal (L > R) PET, N/A SPECT, N/A

The patients had mesial temporal lobe epilepsy with seizures (Szs) recorded from left and right HPC and AMG. All patients had drug-resistant epilepsy (DRE) with failure of at least two antiepileptic medications (ASM). All patients had bilateral IES and Szs. The number of Szs and IESs were greater in the left compared with right HPC and AMG. M, Male; F, female; R, right; L, left; yrs, years; B, bilateral; RF, risk factors; TBI, traumatic brain injury; LOC, loss of consciousness; VNS, vagus nerve stimulation; TL, temporal lobe; FAS, focal aware seizures; FIAS, focal impaired awareness seizures; FTBC, focal to bilateral tonic-clonic seizures. The ASM medications include Cannabidiol (CBD), Carbamazepine (CBZ), Clonazepam (CLZ), Clorazepate (CZP), Cenobamate (CNB), Gabapentin (GBP), Lacosamide (LCM), Lamotrigine (LGT), Levetiracetam (LEV), Lorazepam (LZP), Oxcarbazepine (OXC), Phenytoin (PHT), and Valproic Acid (VPA).

Table 2. Electrode coregistration

	Contact	M1	M2	M3	M4	M5
Lead 1 Left ANT	E ₀	THL	THL	—	THL	THL
	E ₁	THL	THL	THL	THL	THL
	E ₂	THL	THL	THL	THL	THL
	E ₃	THL	THL	THL	THL	THL
Lead 2 Left AMG-HPC	E ₄	PHPC	PHPC	AMG	AMG	—
	E ₅	HPC	PHPC	HPC	HPC	HPC
	E ₆	HPC	PHPC	HPC	HPC	HPC
	E ₇	HPC	HPC	HPC	PHPC	HPC
Lead 3 Right ANT	E ₈	THL	THL	THL	THL	THL
	E ₉	THL	THL	THL	THL	THL
	E ₁₀	THL	THL	THL	THL	THL
	E ₁₁	THL	THL	THL	THL	THL
Lead 4 Right AMG-HPC	E ₁₂	AMG	AMG	AMG	AMG	HPC
	E ₁₃	HPC	HPC	AMG	HPC	HPC
	E ₁₄	HPC	HPC	HPC	HPC	HPC
	E ₁₅	HPC	HPC	HPC	HPC	—

Localization of 16 electrode contacts for subjects M1–5. The four leads were stereotactically targeted to left Thalamus (THL) (contacts E₀, E₁, E₂, E₃), left Amygdala-Hippocampus (AMG-HPC) (contacts E₄, E₅, E₆, E₇), right THL (contacts E₈, E₉, E₁₀, E₁₁), and right AMG-HPC (contacts E₁₂, E₁₃, E₁₄, E₁₅).

Destrieux atlas (Fischl et al., 2004; Destrieux et al., 2010). The final electrode contact localization for impedance analysis was performed with the Lead DBS toolbox (Horn et al., 2019). Table 2 provides the localization information for the electrode contacts used in the study.

RC+S LFP sensing

The LFPs from left and right ANT, AMG, and HPC using four bipolar electrode pairs, sampled at a frequency of 250–500 Hz, were selected for continuous data streaming. The contacts used to create lead-specific bipolar recordings were selected by visual review of LFP data during seizures, resting wakefulness, and sleep–wake transitions. The ANT electrode contacts used for the EBS trials were not used for LFP recordings or further analysis because of the known impact of electrical stimulation on impedance and associated artifacts (Johnson et al., 2005).

LFP analysis

The LFP analysis was performed retrospectively. Previously validated automated algorithms were applied to the long-term intracranial LFP recordings to identify seizures, IES (Sladky et al., 2022) and classify wake-sleep state (Awake, REM, and NREM; Kremen et al., 2019; Mivalt et al., 2022). The algorithm pipeline identifies seizures, IES and sleep–wake behavioral state for consecutive 30 s data segments. The algorithms and their performances were previously reported for four of the subjects (M1–4; Sladky et al., 2022; Mivalt et al., 2022) and here the analysis is extended to include M5. The sleep–wake classifications and seizure events were then synchronized with the impedance measurements for further analysis. Toolboxes and data for automated LFP analysis for detecting IES, seizures, and performing sleep–wake classification are freely available at https://github.com/mselair/best_toolbox.

Seizure and IES detection from continuous LFP recordings

Interictal epileptiform spikes and seizures are electrographic biomarkers of pathologic, epileptogenic brain tissue and are readily identified by human visual review of LFP recordings. Continuous hippocampal LFP recordings from the five subjects were visually reviewed (by G.A.W. and

Table 3. Automated seizure detection and review

Patient	Detected seizure candidates	Expert-confirmed seizures
M1	2060	1035
M2	5616	168
M3	766	642
M4	953	91
M5	12 832	381
Totals	22 227	2317

A hypersensitive threshold was selected for the previously validated CNN-LSTM detector (Sladky et al., 2022). The detector automatically detected 22,227 candidate electrographic seizures, and 2347 of the detected events were visually confirmed as electrographic seizures by human expert review.

N.M.G.) and IES and seizures labeled for subsequent use in training, validating, and testing automated detectors.

We used a previously validated algorithm (Janca et al., 2014; Sladky et al., 2022) for detecting IES transients from LFP recordings. The adaptive IES algorithm enables detecting IES in long-term LFP data with changing background activity commonly encountered in prolonged recordings spanning weeks of time. Here, the gold standard training data were used to set a hypersensitive threshold for all subjects (Table 3).

The intracranial LFP associated with epileptic seizures exhibits characteristic temporal and spectral evolution over a wide frequency range (Fig. 1). We previously described an accurate seizure detector developed using a convolutional neural network (CNN) with long-short-term-memory (LSTM) using short-time Fourier transform of the LFP as the input (Sladky et al., 2022). The CNN-LSTM outputs a seizure probability for 10 s data segments. Gold standard visually reviewed seizures are used for training, validation, and pseudoprospective testing. The seizure detection performance using the CNN-LSTM model was previously reported for subjects M1–4 and here is applied to all five subjects using a hypersensitive threshold to ensure all seizures are detected for the impedance analysis. We visually reviewed all candidate seizure events detected by the hypersensitive automated CNN-LSTM (Table 3).

The temporal distribution of seizures was determined by plotting the circular histogram of seizure onset times for all verified seizures across all subjects. To compare the impedance profiles during seizures with those observed outside seizure events, surrogate nonseizure data were generated. These surrogate nonseizure data were carefully aligned to match the time-of-day distribution observed for actual seizures. The generation of surrogate nonseizure data involved simulating 24 h periods without any seizure activity and ensuring equivalent distributions of times for impedance comparison. Importantly, the surrogate data account for the natural circadian impedance cycles. To create the estimated probability distribution of seizures, we used the rejection method based on the geometric interpretation of probability distribution (Larson and Odoni, 1981). This method allowed us to model the probability distribution of seizure occurrences and evaluate the impedance patterns specific to seizure events against the baseline nonseizure impedance data.

Sleep–wake classification from continuous LFP recordings

Reliable sleep–wake classification was determined by training a subject-specific classifier on simultaneous LFP and gold standard sleep annotations (expert review by E.K.S.) from polysomnography (PSG). For each subject over the course of three nights in the hospital epilepsy monitoring unit, we recorded simultaneous scalp PSG and continuous intracranial LFP data. The PSG signals were scored into standard sleep categories (Awake and REM) and two NREM stages (N2, N3) using American Academy of Sleep Medicine 2012 scoring rules (Berry et al., 2012).

A subject-specific sleep classifier (Naïve Bayes) was trained using the first night of data. The second night was used for validation and the third night for pseudoprospective testing. The Naïve Bayes classifier uses features extracted from the LFP that were previously determined to be useful for sleep–wake behavioral state classification (Kremen et al., 2017, 2019; Mivalt et al., 2022). This approach is limited by the need to record simultaneous PSG and intracranial LFP using the exact LFP and EBS parameters and electrode configurations. In the current study we did not

Table 4. Sleep–wake classification scoring accuracy

Patient	Awake	NREM	REM	Total
M1	0.983	0.935	0.934	0.926
M2	0.951	0.963	0.955	0.935
M3	0.931	0.944	0.944	0.909
M4	0.890	0.913	0.935	0.869
M5	0.947	0.921	0.937	0.903
Overall	0.940 ± 0.030	0.935 ± 0.018	0.941 ± 0.008	0.908 ± 0.023

Results of automated sleep–wake state classification (F1 score) for awake, and REM, NREM sleep categories for subjects M1–5. The automated classifier uses LFP power-in-band inputs, and outputs are classification probabilities. The results for M1–4 were previously published in Mivalt et al. (2022). The first hospital night was used for training, and the second hospital night for validation of the Naïve-Bayes classifier. The results reported here are from the third hospital night with simultaneous polysomnography and intracranial LFP recordings.

have overnight PSG for all EBS configurations and therefore limit the sleep–wake impedance analysis to the initial period (>14 d) of data collection without EBS.

Electrical impedance measurements and analysis

The two-point monopolar electrical impedance was measured from all electrodes in AMG, HPC, and ANT using a square-wave current pulse (0.4 mA, 80 μ s pulse width) over multiple months in five people with drug-resistant epilepsy. The AMG-HPC electrode contacts in seizure onset tissue and ANT electrode contacts used for therapeutic EBS were excluded from impedance analysis because of known acute effect of seizures (Elazar et al., 1966; Fox et al., 2004) and EBS (Lempka et al., 2009; Johnson et al., 2005) on electrode impedance.

The RC+S two-electrode impedance method uses the same electrode contacts for delivering current stimulation and sensing the voltage response. The voltage response to the applied current pulse using the two-point method includes the electrode–tissue interface polarization, created by the electrical stimulation, in addition to the bulk tissue impedance (Ranck, 1966; Lempka et al., 2009). To address the electrode tissue interface contribution caused by electrolyte polarization, the four-electrode method has been used in animal studies (Ranck, 1966; Logothetis et al., 2007). This method involves using one pair of electrodes to deliver the current and a separate pair of electrodes to measure the voltage response (Fig. 2). However, it is important to note that the RC+S device, as well as other human investigational and approved devices that we are aware of, currently do not support four-point impedance measurements. To investigate and compare the differences between two-point and four-point measurements, we conducted a series of benchtop experiments. These experiments involved using a composite material consisting of saline and microbeads, which exhibit an effective impedance similar to the reported values found in mammalian brain (Ranck, 1966; Logothetis et al., 2007; Miceli et al., 2017).

Furthermore, we used this composite model to compare the impedance measurements obtained with the two-point square-wave pulse current probe the RC+S device uses with the results obtained from the four-electrode and two-electrode measurement using sinusoidal stimulation currents.

Saline/microbead impedance measurements

We conducted benchtop experiments using saline and saline/microbead composites (Fig. 2). The aim of these experiments was to directly compare two-point and four-point electrode impedance measurements over a range of sinusoidal current frequency (1–5000 Hz) with two-point RC+S impedance measurements using a single square-wave pulse. A Medtronic 3387-lead (four contacts each with 4.7 mm² surface area) submerged in the center of a plastic cylinder reservoir (radius, 5 cm; height, 40 cm) filled with saline (0.9% sodium chloride solution at 22°C; 68.9 Ω -cm), or a saline/microbead composite (volume fractions 36% saline and 64% microbeads (80–120 μ m; Sauerheber and Heinz, 2015; Savtchenko et al., 2017, 2021) was used for the experiments. To simulate monopolar electrical impedance measurements, a single electrode, contact on the 3387-lead, was used as the cathode, and a large surface area electrode at the bottom of the cylinder was the anode (simulating the

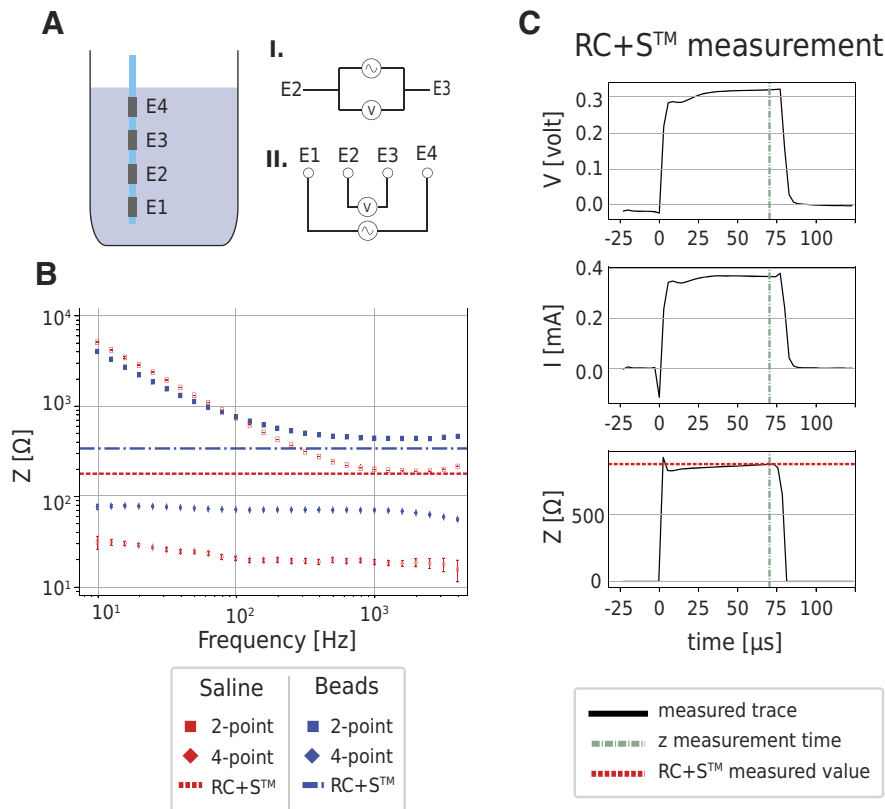


Figure 2. Impedance measurements in saline/microbead composites. **A**, A benchtop phantom fixture was used for testing two- and four-point impedance measurements in saline/microbead composites. For two-point monopolar measurements, current is injected into the sample medium using the 3387-lead contacts as the cathode (E_1), and the anode is a large surface area contact (E_0) at the bottom of the cylindrical container. The two-point measurement uses the same electrode contacts (E_2 and E_3 or E_0) for both electrical stimulation and voltage sensing. The four-point impedance measurement uses different electrodes for stimulation (E_1 and E_4) and sensing (E_3 and E_2). The four-point measurements eliminate the interface electrode–electrolyte polarization, related to electrical stimulation, from the voltage measurements and provides a measurement of the medium. **B**, Impedance measured using sinusoidal currents in saline and saline/microbead composites (1–4000 Hz). The two-point measurements are dominated at low frequency (<500 Hz) by the frequency-dependent capacitive double layer related to the electrolyte polarization at the electrode–electrolyte interface in both saline (red squares) and saline/microbead (blue squares). The four-point impedance measurement, using different electrodes for current injection and voltage response sensing, yields a purely resistive impedance with no frequency dependence (10–4000 Hz). The RC+S impedance measurement results are shown for comparison as a blue dashed line (saline/microbead) and red dashed line (saline). **C**, The RC+S calculates impedance using Ohm's law, $Z = V/I$, where I is the injected current (0.4 mA, 80 μs pulse width) and V is the voltage response measured at 70 μs. The voltage recording using two-point measurement shows the voltage response to the impulse current (0.4 mA, 80 μs pulse width) with charging of the electrode–electrolyte double layer capacitor, which reaches an asymptotic voltage within ~ 50 μs. The RC+S impedance measurement can be seen to correlate with ~ 1000 Hz sinusoidal current input.

large RC+S surface area of $\sim 5.4 \times 10^3$ mm²). In addition, two-point bipolar measurements using the inner two contacts of the 3387-lead were used for stimulation and recording. The four-point measurements used the outer two contacts of the 3387-lead for injecting current and the inner two contacts for recording the voltage response. A National Instruments USB6251 signal generator and a NPI electronics ISO isolation unit (<https://www.npielectronic.com>) were used to deliver 0.4 mA sinusoidal currents over a wide frequency range (1–5000 Hz). The voltage drop across the measurement electrodes was recorded using a Neuralynx cube acquisition system (<https://www.neuralynx.com>). The impedance for each frequency (f) was calculated from Ohm's law $Z_{\text{eff}}(f) = V_{\text{measured}}(f)/I_{\text{stim}}(f)$ and averaging the measurement at each frequency over >25 cycles.

The two-point RC+S impedance measurement uses a single current pulse (0.4 mA, 80 μs pulse-width) to probe the tissue and calculates the impedance from Ohm's law $Z_{\text{eff}} = V_{\text{measured}}/I_{\text{stim}}$ with the voltage measured at 70 μs, near the end of the 80 μs current test pulse (Fig. 2C). The two-point RC+S can be directly compared with the two- and four-point impedance measurements that use sinusoidal currents (Fig. 2B).

Human brain impedance analysis

The impedance time series (sampled every 5–15 min) in the five subjects were resampled with a 30-min-long moving average window with a step of 10 min and bandpass filtered between 30 min to 100 d with low- and high-pass finite impulse response, zero phase shift filters of 1,001st order.

Polar impedance plots with the histograms of the minimum and maximum impedance value recorded over each 24 h (day/night) cycle were tested for nonuniform circular distributions using the Kuiper (1960) test ($*p < 0.05$, $**p < 0.01$, $***p < 0.001$).

Multiscale impedance cycle analysis

The continuous wavelet transform (CWT) was used to investigate brain impedance cycles with ultradian (<24 h), circadian (~ 24 h), and infradian (>24 h) periodicities. The CWTs were implemented in MATLAB software (Morlet wavelets and L2 normalization). The Thomson F test multitaper scheme (Thomson, 1982) was used to test for significance of oscillations with a 5 d moving window used for ultradian and circadian cycles and a 100 d moving window (step of 5 d) for infradian cycles. The presence of ultradian, circadian, and infradian frequency band oscillations were identified using preprocessed impedance signals (z score and downsampled to 48 samples/day). The periodicity test in ultradian band for each 5 d signal segment was investigated using the time-half-band product (TW) set at three ($TW = 3$), and the number of tapers (K) was five ($K = 5$), resulting in the frequency resolution of $2W = 1.2$ (or $2W = 0.06$) cycles/day. In ultradian band, frequency of interest (FOI) was chosen from $23/24 = 0.96$ h/cycle to 6 h/cycle with an incremental step of 15 min; in infradian band, the FOI was from 2.5 d/cycle to 30 d/cycle with an incremental step of 15 min. At each fixed frequency, the F test was set at the level of the upper 99% ($p = 0.01$) percentage point of the F

Table 5. Sleep characteristics

	M1	M2	M3	M4	M5	Overall
Sleep onset [h:min]	1:18 A.M. \pm 0:57	1:18 A.M. \pm 2:22	10:42 P.M. \pm 0:38	10:42 P.M. \pm 0:37	0:24 A.M. \pm 2:24	11:50 P.M. \pm 1:47
Sleep offset [h:min]	10:03 A.M. \pm 0:55	10:33 A.M. \pm 3:1	7:39 A.M. \pm 0:32	8:06 A.M. \pm 0:51	8:05 A.M. \pm 2:17	8:48 A.M. \pm 1:51
Sleep duration [h:min]	8:46 \pm 1:01	8:51 \pm 2:56	8:57 \pm 0:38	9:24 \pm 0:50	7:39 \pm 1:7	8:56 \pm 1:25
<i>N</i> sleep cycles	5.13 \pm 2.43	2.78 \pm 2.47	3.90 \pm 2.55	3.67 \pm 2.07	5.00 \pm 2.00	4.04 \pm 2.50
NREM epoch duration [min]	18.46 \pm 29.36	28.16 \pm 40.59	20.53 \pm 33.04	16.89 \pm 8.71	23.20 \pm 27.02	19.93 \pm 31.91

The average sleep onset times, offset times, number of NREM-REM cycles, and duration of NREM epoch are tabulated for all subjects. The average sleep duration for all five subjects is 08:56 \pm (01:25) with 4:04 \pm 2.50 cycles. The average NREM epoch duration is 19.93 \pm 31.91 min. The table highlights the variability across subjects and within each subject.

distribution with 2 and 2K-2 = 8 degrees of freedom under the null hypothesis of no spectral line, leading to the critical value of 8.65.

Sleep–wake state dependence of impedance

We compared the three behavioral categories on a group and subject level using a statistical two-tailed Mann–Whitney test ($p < 0.05$, Bonferroni correction for multiple observations). The continuous behavioral state classifications were also reviewed for periods of daytime sleep (>30 min duration), and in four of five subjects we identified daytime naps making analysis and comparison of sleep impedance during daytime naps and overnight sleep possible.

Summary of LFP and impedance data

The RC+S provides streaming of four LFP channels (250–500 Hz sampling) and 16 monopolar impedance values (0.001–0.003 Hz sampling) to the patient's tablet computer for storage. When there is either cellular or wireless connectivity available the data are transferred from patient's tablet to a cloud database (Kremen et al., 2018). The sampling frequencies were determined as a compromise between data quality, wireless data transmission, and device battery limitations. The LFP and impedance data were collected during an ongoing investigational device clinical trial that is testing different ANT EBS paradigms for drug-resistant epilepsy that include (1) no EBS baseline, (2) low-frequency EBS (2 and 7 Hz continuous), and (3) high-frequency EBS (125 Hz continuous, duty cycle, 1 min on and 5 min off, and responsive).

Because of the acute effects on tissue impedance, we exclude (1) data from the initial 14 d after surgical implant (Lempka et al., 2009; Sillay et al., 2013), (2) data within 12 h before and after seizures (Elazar et al., 1966; Binder et al., 2004; Fox et al., 2004), (3) data from electrode contacts located in seizure onset zone, (4) data from electrode contacts used for EBS (Lempka et al., 2009; Johnson et al., 2005), and (5) data from electrode contacts with high impedance (>5000 Ω). This left 45.00% (36/80) of the electrode contacts (5 AMG, 14 HPC, 17 ANT) for subsequent analysis of impedance and association with sleep–wake behavioral state.

The complete dataset available for analysis included at least 150 d for each patient (M1, 828 d; M2, 549 d; M3, 346; M4, 549; M5, 150 d). We excluded days with poor telemetry and <70% data because of the possibility of missing seizures, leaving 1456 continuous 24 h epochs from 5 subjects (291 \pm 198 24 h epochs). The analysis of sleep–wake impedance changes was focused on the 30 d period before starting EBS. During the initial period without EBS there were 299 data segments (30–90 min durations) from the 36 electrode contacts without seizure activity for at least 24 h annotated across the five patients and three behavioral categories—Awake, NREM, REM (M1, 30/21/22; M2, 20/19/18; M3, 15/14/13; M4, 22/27/29; M5, 12/19/18) for analysis.

Data availability

All data and analysis code are available on reasonable request from the authors and from https://github.com/mselair/best_toolbox.

Results

The LFP recordings from the five subjects were used as input to automated algorithms for detecting seizures and classifying sleep–wake state (Tables 3, 4). The characteristics of sleep show a wide range of features including sleep onset, offset and duration. The number of NREM-REM cycles over the dataset analyzed

shows a significant variability within patients and across the group (Table 5). All five subjects had independent bilateral mesial temporal lobe IES and seizures. The IES rate and seizure counts are significantly higher in the left compared with right mesial temporal lobe ($p < 0.001$; Table 1).

Saline/microbead composites were used to compare two-point RC+S impedance measurements that use a square-wave current pulse with both two-point and four-point impedance measurements using sinusoidal currents (Fig. 2). The microbead volume fraction was adjusted to approximate the impedance measured in mammalian and human brain using two-point measurements (Lempka et al., 2009). The qualitative difference between two-point and four-point impedance measurements is the absence of frequency dispersion in the impedance over the range of ~1–1000 Hz with the four-point measurement. In contrast the two-point measurement shows frequency dispersion over this range consistent with a capacitive term because of the Helmholtz double layer at the stimulation electrode–electrolyte interface (Bard and Faulkner, 2001). Above ~2000 Hz the two-point impedance is purely resistive without dispersion. The two-point RC+S voltage response to the 0.4 mA, 80 μ s square-wave probe shows behavior consistent with charging a capacitive interface over the initial ~40 μ s and then asymptotes before the measured response at 70 μ s and yields an impedance similar to the impedance measured with sinusoidal currents between 1000 and 4000 Hz (Fig. 2B, dashed line). In this frequency range the two-point measurement is also purely resistive without frequency dispersion. The difference between four- and two-point measurements highlight the significant confound introduced by the electrode–media interface impedance that is in series with the brain tissue impedance when the electrical current stimulation and voltage sensing are performed with the same electrodes.

Human brain impedance

Impedance was measured in five people with drug-resistant mesial temporal lobe epilepsy over multiple months using the RC+S monopolar two-point current pulse method with periodic sampling (every 5–15 min) in AMG, ANT, and HPC. The impedance increases after surgery but reaches a stable value after ~14 d (Fig. 3B), consistent with previous studies (Lempka, 2009; Sillay et al., 2013). All subsequent analysis was performed using data at least 15 d after implant to avoid the acute effects.

Seizures are known to effect brain impedance (Elazar et al., 1966; Fox et al., 2004) and ECS volume (Binder et al., 2004), and to address this possible confound we used a hypersensitive seizure detector combined with expert visual review to label all seizures in the LFP data. As previously reported for temporal lobe epilepsy (Durazzo et al., 2008; Hofstra and de Weerd, 2009) the seizures primarily occur in either the morning or late afternoon in all subjects M1–5 (Fig. 4A). The impedance in the 24 h surrounding seizures was increased when compared with days without seizures (Fig. 4B). To eliminate the confound of seizure-

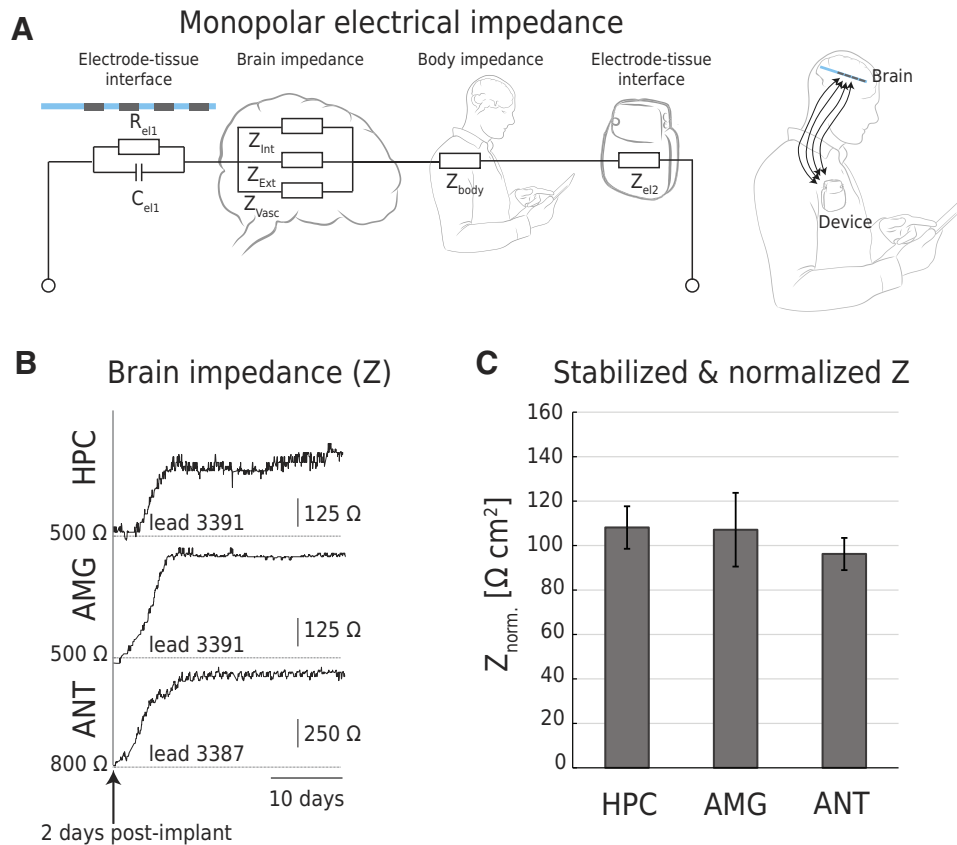


Figure 3. Human brain impedance. **A**, Circuit model for monopolar brain impedance measurements. The impedance contributions include the electrode–tissue interface, multiple brain compartments (ECS, vascular, cellular), body, and device–tissue impedance. **B**, Example impedance traces from electrodes targeting HPC, AMG, and ANT anatomic locations within the first 4 weeks (~ 30 d) postimplant. Postimplant impedance shows an increasing trend that asymptotes to a stable mean value after ~ 14 d. **C**, Normalized stable impedance for the anatomic locations. The stabilized Z values were estimated as the mean of the raw impedance between 15 and 21 d after implant and are scaled by multiplying by the electrode contact surface area. The normalized stable measures were aggregated across five subjects (M1–5) for each location. Error bar indicates ± 1 SD. The asymptote values of AMG, ANT, and HPC impedance are similar when corrected for electrode surface area.

related impedance changes, the ± 12 h data segments around seizures are excluded from all subsequent analysis.

Group-level analysis (Fig. 5B) reveals that the average impedance increases throughout the day in HPC, AMG, and ANT. The average impedance peaks at 7:51 P.M. \pm 04:33, 9:10 P.M. \pm (05:12), and 6:25 P.M. \pm (04:57) in the evening for HPC, AMG, and ANT respectively. The average impedance decreases during the night, reaching its lowest point at 6:49 A.M. \pm (03:49), 6:20 A.M. \pm (04:20), and 8:36 A.M. \pm (04:46). The average impedance difference between the daytime maximum and nighttime minimum was $29.29 \pm 12.39 \Omega$ for HPC, $29.87 \pm 19.61 \Omega$ for AMG, and $36.72 \pm 20.32 \Omega$ for ANT (Table 6). Figure 5 shows the group-level and individual subject circular histograms of the maximum impedance (orange) and minimum impedance (brown).

Multiscale impedance oscillations

In addition to ~ 24 h cycles captured with the polar plots (Fig. 5) there are shorter- and longer-cycle periods in the impedance time series. Analysis using CWT of AMG, ANT, and HPC impedance time series shows multiscale oscillations with ultradian, circadian, and infradian periodicities (Fig. 6). The circadian oscillation is highly regular over the duration of the entire recording (Fig. 6A). Statistical testing with the Thomson *F* test multitaper scheme (Thomson, 1982; Percival and Walden, 1993) was used to identify ultradian, circadian,

and infradian oscillations in the impedance time series [Fig. 6A, bottom, detection of significant ultradian (yellow dots), circadian (red dots), and infradian (blue dots) oscillations]. Ultradian cycles are not well visualized in the average amplitude index power density calculated from the long impedance time series (Fig. 6A, middle right, amplitude index in gray), but when investigated in shorter data segments the ultradian cycles are more readily visualized (Fig. 6B). The variability of sleep onset and offset times and sleep duration (Table 5) all contribute to the reduced average amplitude index power density.

When the oscillation detections are aggregated, the cycle periodicities occurring most frequently can be identified (Fig. 6D). Note that in the ultradian band centered at 1.5–1.7 h/cycle is increased, which is the average human NREM-REM sleep cycle (1.6 h/cycle, or 5 cycles per 8 h).

Impedance and behavioral state (wakefulness, NREM, and REM sleep)

In total, 299 data segments from the 36 right-hemisphere electrode contacts without seizure activity for at least 24 h were identified across the five patients and three behavioral states. The impedance was lower in NREM sleep compared with wakefulness and REM sleep (Fig. 7; Table 7). The impedance in AMG, ANT, and HPC reaches its minimum value in NREM, intermediate value in REM, and highest value in wakefulness (Fig. 7B,C).

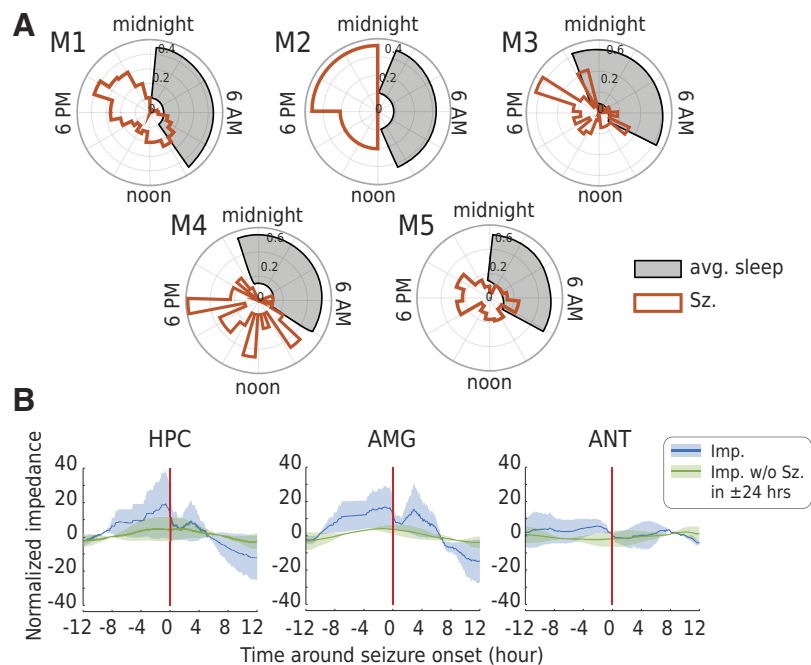


Figure 4. Temporal profiles of seizures and acute impedance changes. **A**, Circular histograms were used to illustrate the distribution of seizure onset times (red histograms) and sleep periods (gray filled) over a 24 h clock for each subject. The distribution of seizures as a function of time of day shows that seizures primarily occur during daytime and exhibit a bimodal distribution. A diurnal bimodal distribution of temporal lobe seizures was previously reported for temporal lobe epilepsy (Durrázo et al., 2008). **B**, Impedance measurements from AMG, ANT, and HPC during the ± 12 h surrounding spontaneous seizures (blue line) were compared with days without seizures (green line). The data demonstrate an increase in average impedance on days with seizures. Raw impedance time series were segmented to ± 12 h around the seizure onset times. The mean value of the impedance was subtracted from each segment to obtain the normalized impedance. The normalized impedance time series were aggregated and smoothed using a 2.4 h moving window. For each subject, the smoothed normalized impedances were aggregated, and the mean value per anatomic location (ANT, AMG, HPC) was calculated. The red vertical line indicates the onset time of seizures (for blue traces) or surrogate segments without seizures within 24 h (green traces). The surrogate segments without seizures were selected to match the time-of-day temporal distribution of actual seizure events. The blue curve represents the mean value of seizure-related normalized impedance, incorporating all seizures, whereas the green curve represents the mean value of normalized impedance from 24 h segments without any seizures. The distribution of time of day of impedance data segments without seizures (green) is matched to the distribution of time of day of actual seizure events to account for baseline circadian changes in impedance. The shaded areas around the means indicate ± 1 SEM, representing the uncertainty across the subjects ($n = 5$).

Four of the five subjects also took afternoon naps (nap onset 2:06 P.M. ± 1.2 h). Impedance in NREM sleep during naps was analyzed (M1, 7; M2, 1; M3, 7; M4, 3) and compared with the wakefulness impedance in the hour before the nap. The nap NREM sleep impedance is decreased when compared with wakefulness in HPC, AMG, and ANT (Fig. 7C).

The average baseline total impedance in the AMG, HPC, and ANT during wakefulness was $753.58 \pm 80.23 \Omega$, $892.74 \pm 97.27 \Omega$, and $1268.28 \pm 63.17 \Omega$, and during NREM sleep was reduced to $730.11 \pm 77.00 \Omega$, $874.30 \pm 99.49 \Omega$, and $1246.61 \pm 54.35 \Omega$, respectively (Fig. 7D). The average circadian minimum to maximum impedance changes, ΔZ , in AMG, HPC, and ANT are $29.87 \pm 19.61 \Omega$, $29.29 \pm 12.39 \Omega$, and $36.72 \pm 20.32 \Omega$, respectively (Table 6).

Discussion

The total impedance consists of the electrode–tissue impedance in series with the brain tissue impedance (Figure 3), and with the two-point measurements the electrode–tissue impedance dominates the total impedance. This is evident in the benchtop experiments (Fig. 2) in both saline and saline/microbead composites where the four-point impedance measurement is at least an order of magnitude smaller than the two-point measurement. Similarly, based on the benchtop saline/microbead experiments, we expect the human brain electrode–tissue impedance is >10 times greater than the isolated brain impedance (Figs. 2B, 3B). The circadian cycle impedance change typically represents $<5\%$

of the total impedance. But despite the small relative impedance change, the impedance cycles with circadian periodicity are often visible in the raw data (Fig. 3B).

The human AMG, ANT, and HPC show complex temporal dynamics with multiscale oscillations spanning hours to weeks (Figs. 1, 5, 6). The impedance in the limbic structures reaches the lowest value in NREM, an intermediate value in REM, and is highest values during wakefulness (Fig. 7). The impedance rises on average throughout the day during wakefulness, reaching a maximum in the evening before sleep and then decreases over the night reaching a minimum value in the early morning before awakening (Fig. 5). In sleep the impedance cycles in association with sleep state transitions between NREM and REM sleep (Fig. 7).

Sleep–wake state transitions appear to generate the observed impedance cycles with characteristic oscillations anchored by a highly stable, dominant 24 h cycle. Compared with the circadian cycles, the ultradian and infradian cycles show more variability (Fig. 6). The variability of sleep characteristics (Table 5), NREM–REM cycles (average 4.04 ± 2.50 cycles), and NREM epoch duration (19.93 ± 31.91 min) will tend to smear out the CWT color maps for the ultradian periods. The significance testing on 5 d windows, however, continues to show cycles with ultradian periods that are consistent with NREM–REM cycles. We propose the multiscale impedance cycles represent normal brain physiology given that this analysis is focused on the less-epileptogenic brain regions and excludes seizures. We selected electrodes and data segments not involved in seizure onset and analyzed 24 h data

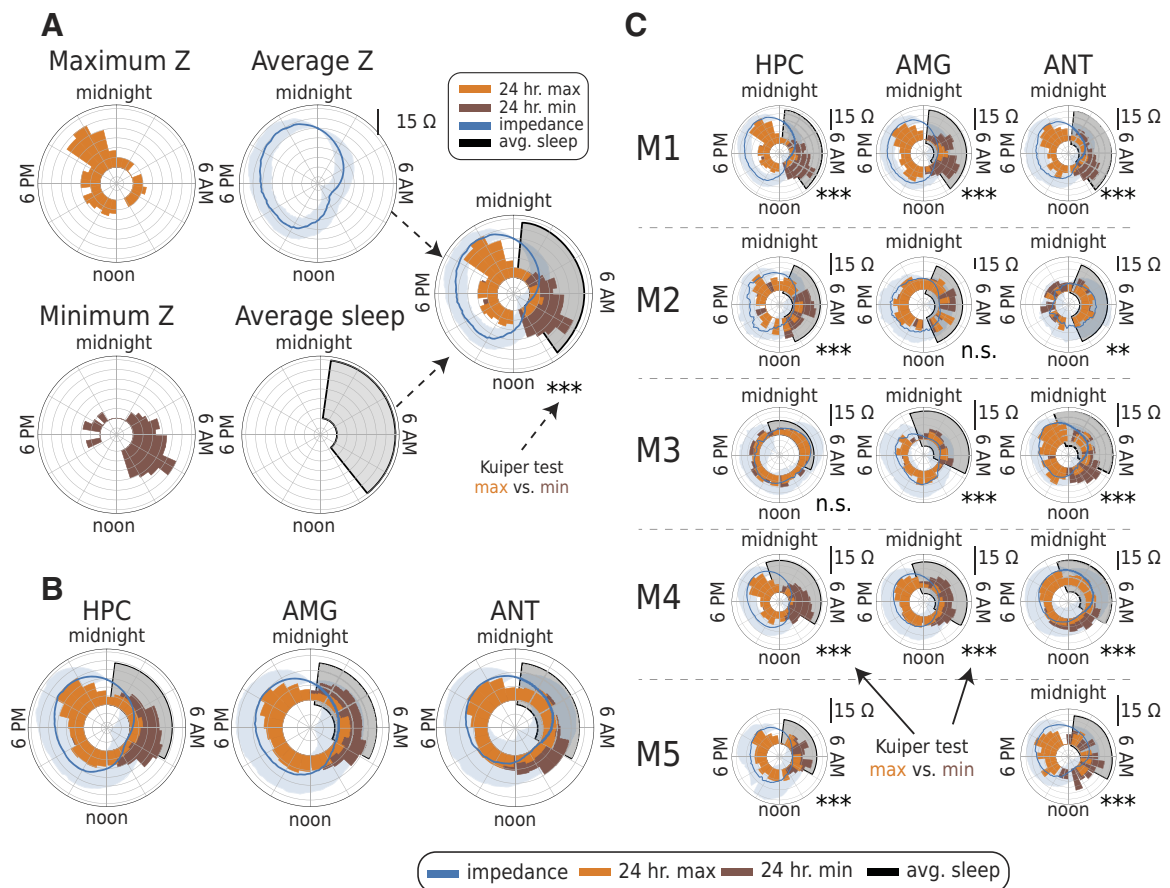


Figure 5. Twenty-four-hour impedance cycles. Circular histograms of the impedance maximum (orange) and minimum (brown) are overlaid with average impedance (blue line) and sleep (shaded gray). **A**, Top left, Circular histogram of representative of 24 h impedance maximum values. Bottom left, Circular histogram of representative of 24 h impedance minimum values from same subject (M1). The maximum impedance values occur in late daytime hours during wakefulness. The minimum impedance values are in the early morning hours during sleep. Top right, The running average impedance using a 4 h window with 2 h overlaps show the diurnal pattern with impedance increased during daytime and decreased during nighttime. Bottom middle, The average period of sleep determined from the automated sleep–wake classifier (gray filled). Right, Composite polar plot containing (1) minimum/maximum (min/max) impedance histograms, (2) average impedance, (3) sleep period. **B**, The group-level composite polar plots from HPC, ANT, and AMG averaged across all subjects demonstrates that the min/max impedance values over 24 h periods of day/night are not uniformly distributed. **C**, Composite polar plots for individual subjects M1–5 over multiple months show the average impedance increases during wakefulness and decreases during sleep (blue curve). The HPC, AMG, and ANT histograms show the impedance reaches maximum values in the evening during wakefulness and minimum values during the night and early morning sleep before waking. Subject M2 displays less consistent 24 h cycles. The circular histogram distributions of the minimum (brown) and maximum (orange) values of the 24 h impedance cycle were tested using the circular Kuiper test and show strong phase preferences for night and day ($p < 0.05$, $**p < 0.01$, $***p < 0.001$). Subject M5 did not have a right AMG electrode because of a technical issue during surgery.

Table 6. Circadian impedance cycles

Subject	Location	Time of Z_{\min}	Time of Z_{\max}	Magnitude Z [Ω] change	Kuiper p value
M1	HPC	07:40 A.M. \pm 02:44	08:49 P.M. \pm 3:30	35.55 \pm 8.93	<0.001
	AMG	06:54 A.M. \pm 02:39	07:12 P.M. \pm 4:05	35.55 \pm 21.44	<0.001
	THL	07:30 A.M. \pm 03:10	08:02 P.M. \pm 4:04	32.90 \pm 15.77	<0.001
M2	HPC	07:09 A.M. \pm 03:29	08:50 P.M. \pm 6:10	31.74 \pm 11.09	<0.001
	AMG	05:18 A.M. \pm 04:41	08:16 P.M. \pm 7:04	65.43 \pm 33.30	n/a
	THL	10:34 A.M. \pm 05:42	06:57 A.M. \pm 5:09	43.10 \pm 24.88	<0.01
M3	HPC	03:51 P.M. \pm 08:39	07:32 A.M. \pm 7:21	35.57 \pm 16.58	n/a
	AMG	04:33 A.M. \pm 04:44	01:56 P.M. \pm 6:02	23.31 \pm 8.94	<0.001
	THL	08:30 A.M. \pm 04:16	07:57 P.M. \pm 4:54	32.23 \pm 12.80	<0.001
M4	HPC	06:27 A.M. \pm 03:10	07:26 P.M. \pm 3:30	24.75 \pm 8.58	<0.001
	AMG	06:29 A.M. \pm 04:49	06:29 P.M. \pm 4:32	24.55 \pm 11.21	<0.001
	THL	09:44 A.M. \pm 04:55	10:09 P.M. \pm 5:03	40.81 \pm 22.72	<0.001
M5	HPC	05:46 A.M. \pm 03:31	07:09 P.M. \pm 5:26	28.44 \pm 19.93	<0.001
	THL	07:40 A.M. \pm 03:37	07:33 P.M. \pm 4:13	23.00 \pm 6.84	<0.001
Average	HPC	06:49 A.M. \pm 3:49	07:51 P.M. \pm 4:33	29.29 \pm 12.39	<0.001
	AMG	06:20 A.M. \pm 4:20	09:10 P.M. \pm 5:12	29.87 \pm 19.61	<0.001
	THL	08:36 A.M. \pm 4:46	06:25 P.M. \pm 4:57	36.72 \pm 20.32	<0.001

The average time of minimum and maximum impedance values, and the magnitude of the minimum and maximum impedance difference is tabulated. All subjects had significant 24 h impedance cycles with the minimum impedance in the morning hours and maximum impedance in the evening hours. The statistically significant values in bold are for nonuniform circular distributions (Kuiper, 1960).

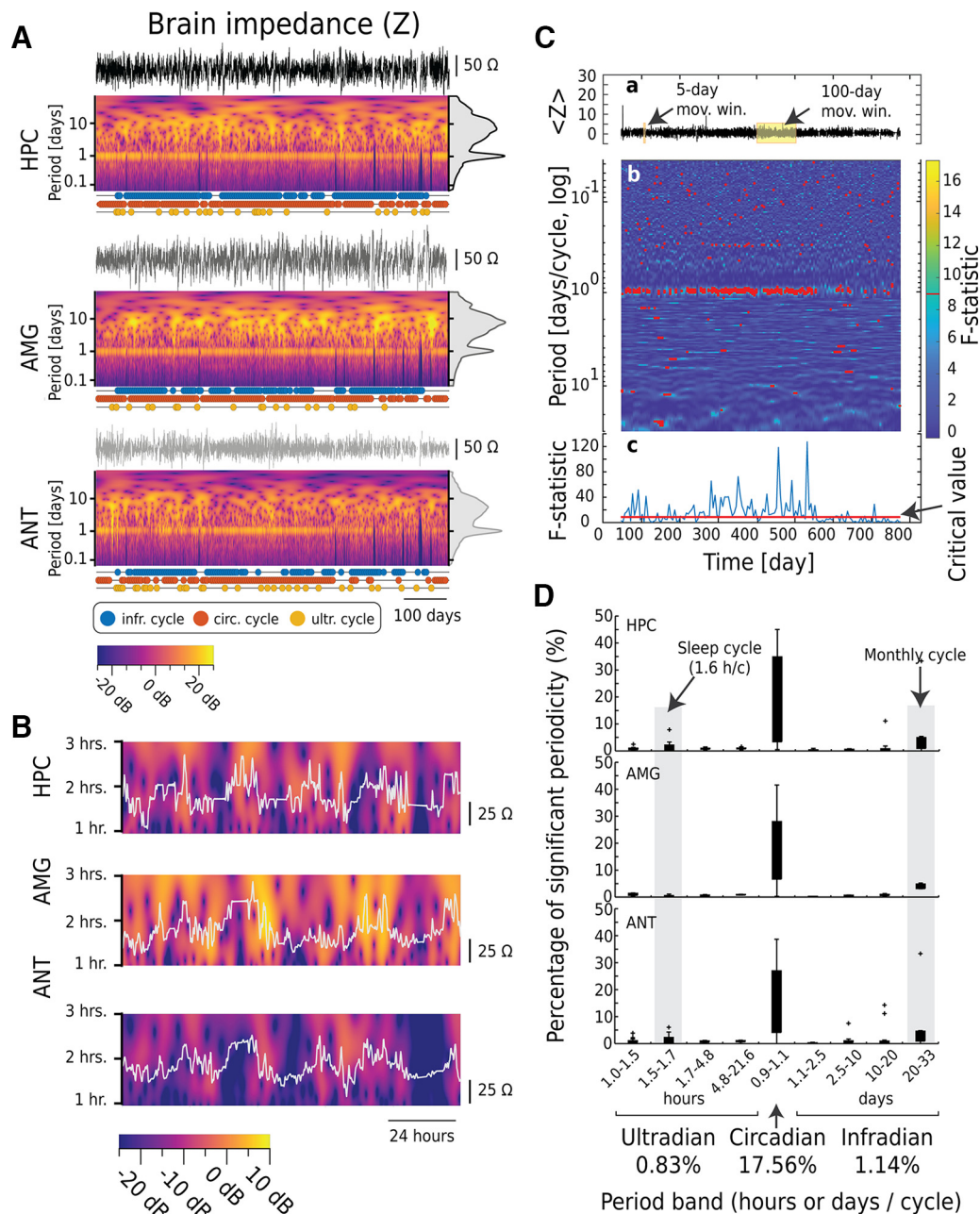


Figure 6. Multiscale rhythms of human brain impedance. The AMG, ANT, and HPC impedance time series exhibit multiscale cycles with ultradian, circadian, and infradian periods. **A**, Top to bottom, Displays for the HPC, AMG, and ANT impedance time series and analysis. Top, Raw impedance time series. Middle, CWT of impedance time series demonstrating multiscale oscillations. The circadian period (1 d) is most prominent with little variability over the multiple-month record. Right, Amplitude index (gray) shows the high-power, narrow circadian peak that can be compared with the broad more diffuse ultradian and infradian bands. Bottom, Significance test for ultradian (yellow dots), circadian (red dots), and infradian (blue dots) cycles identified using the *F* score test. **B**, Blowup of CWT over a shorter evaluation window of 3 d provides a clearer visualization of ultradian oscillations (~1.25–3 h) that are not visually evident in the long-term amplitude index and CWT. **C–c**, Statistical testing with Thomson *F* test multitaper scheme (Thomson, 1982; Percival and Walden, 1993) was used to identify significant ultradian, circadian, and infradian impedance cycles. **a**, The presence of cycles with ultradian and circadian periods was investigated using a 5 d moving window (*z* score and downsampled to 48 samples/day and moving step of 5 d). A 100 d moving window (moving step of 5 d) was used to investigate cycles in infradian band. **b**, Thomson *F* test based on the multitaper scheme to test the periodicity at the F0s. **c**, The *F* test was set at the level of the upper 99% ($p = 0.01$) where the red dash on the scale color bar (right) indicates the *F* statistic above the critical value. **D**, Box plots of percentage of significant impedance cycles in ANT, AMG, and HPC. We examined the percentage of significant ultradian (1.0–1.5, 1.5–1.7, 1.7–4.8, and 4.8–21.6 h/cycle), circadian (0.9–1.1 d/cycle), and infradian (1.1–2.5, 2.5–10, 10–20, and 20–33 d/cycle) cycles at each anatomic location under examination. We aggregated the values across subjects and present them as box plots at each location per period band. Note that the fundamental frequency of the sleep cycle (1.6 h/cycle or 5 cycles per 8 h) is centered at the ultradian band of 1.5–1.7 h/cycle. The shaded area highlights the period bands that have higher proportions of significant periodicity in addition to the circadian cycle.

periods without any seizure activity. The variability of NREM and REM sleep duration and state transitions observed over the multiple-month ambulatory recordings likely underlies the ultradian impedance cycle variability. This variability may be amplified here by the well-known sleep fragmentation in people with epilepsy (Bazil,

2017). Regarding the observed impedance cycles with infradian periods (>24 h), we did not find a behavioral correlate for these impedance cycles, but similar long-term cycles in pathologic brain electrical activity and seizures are known to occur in epilepsy (Baud et al., 2018; Gregg et al., 2020, 2021; Karoly et al., 2021).

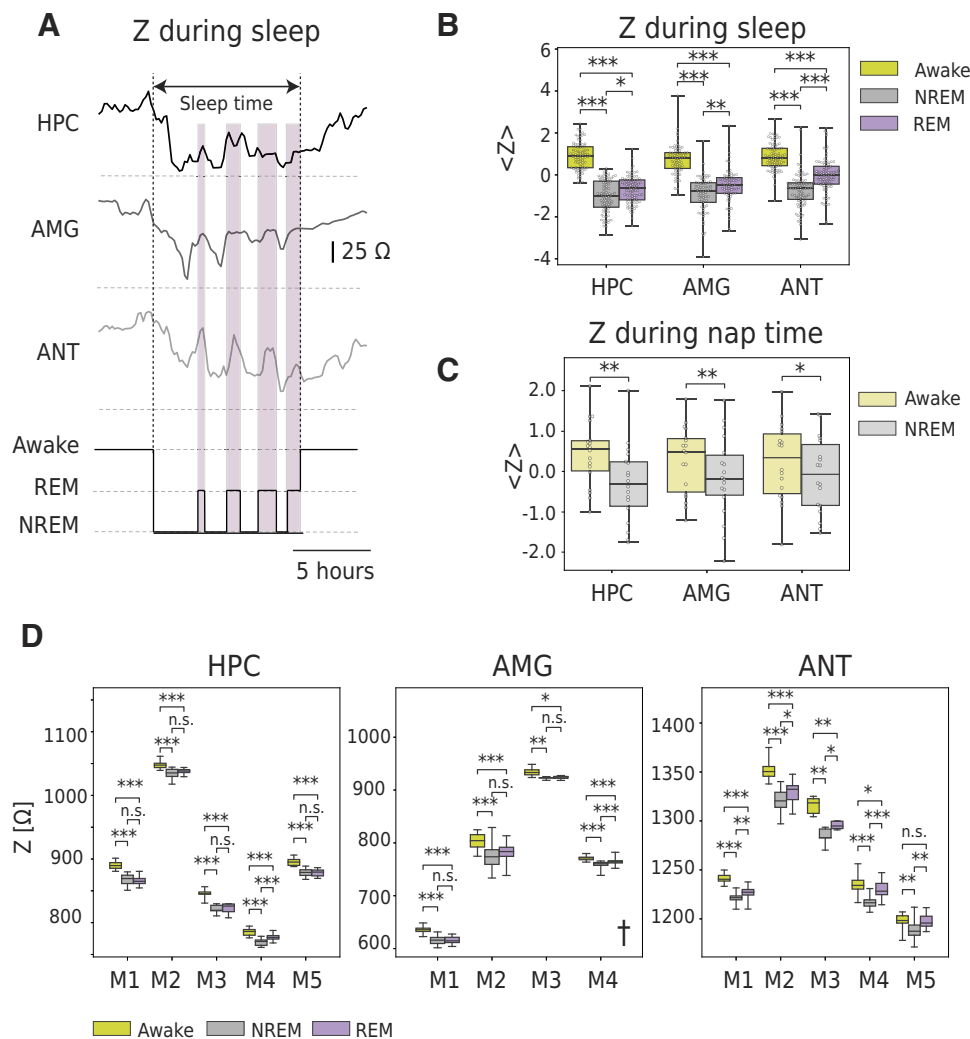


Figure 7. Sleep–wake state dependence of human brain impedance. Limbic brain impedance depends on sleep–wake state. **A**, Impedance changes over a single night during a hospital stay with gold standard sleep–wake classifications from polysomnography, including wakefulness and four cycles of NREM and REM sleep from subject M5. The impedance decreases during the transition from wakefulness to NREM sleep and increases during transitions from NREM to REM. **B**, Group-level analysis (M1–5) shows that the average impedance in HPC, AMG, and ANT is lowest during NREM sleep, intermediate in REM sleep, and highest in wakefulness. **C**, Similarly, in subjects (M1–4) taking daytime naps including at least 30 min of NREM sleep, the HPC and AMG impedance is decreased in NREM sleep compared with wakefulness before the nap. These results during daytime naps further support that impedance cycles are related to dependence on the sleep–wake behavioral state. **D**, At the individual subject level, the ANT, AMG, and HPC impedance is greater during wakefulness compared with NREM sleep in all subjects, and it is greater than REM sleep for all subjects except M5. The impedance in the ANT is greater in REM sleep compared with NREM for all subjects but only reaches significance in the HPC and AMG for M4. The impedance difference between wakefulness and REM sleep is smaller compared with the difference observed between NREM and wakefulness or NREM and REM sleep ($*p < 0.05$, $**p < 0.01$, $***p < 0.001$; Mann–Whitney test with Bonferroni correction for multiple observations). †AMG data were not available for M5.

Table 7. Impedance changes during sleep–wake behavioral state transitions

Behavioral state (sleep–wake)		M1 [Ω]	M2 [Ω]	M3 [Ω]	M4 [Ω]	M5 [Ω]	Overall [Ω]
Awake – NREM	HPC	22.45 \pm 7.22	12.91 \pm 6.11	24.15 \pm 7.22	15.48 \pm 5.43	17.19 \pm 5.77	17.84 \pm 6.68
	AMG	20.49 \pm 6.89	30.78 \pm 19.02	11.63 \pm 5.21	11.84 \pm 4.95	—	20.15 \pm 12.01
	ANT	20.22 \pm 4.83	30.10 \pm 9.69	31.54 \pm 8.38	17.77 \pm 6.50	7.84 \pm 7.96	20.28 \pm 8.72
Awake – REM	HPC	24.22 \pm 6.13	10.01 \pm 4.63	23.29 \pm 8.06	8.50 \pm 4.97	16.97 \pm 5.38	15.61 \pm 6.55
	AMG	20.03 \pm 6.08	25.12 \pm 17.15	10.66 \pm 5.66	5.88 \pm 4.79	—	16.03 \pm 10.87
	ANT	14.81 \pm 5.16	20.55 \pm 9.54	20.23 \pm 6.12	4.62 \pm 7.74	−0.92 \pm 10.04	10.67 \pm 8.71
NREM – REM	HPC	1.77 \pm 7.57	−2.90 \pm 5.38	−0.85 \pm 7.62	−6.98 \pm 5.12	−0.22 \pm 5.54	−2.22 \pm 6.91
	AMG	−0.46 \pm 7.45	−5.66 \pm 21.60	−0.96 \pm 2.77	−5.97 \pm 5.94	—	−4.12 \pm 13.80
	ANT	−5.41 \pm 5.69	−9.56 \pm 10.78	−11.30 \pm 6.04	−13.15 \pm 6.57	8.51 \pm 7.37	−9.61 \pm 9.83

Average impedance change between wakefulness, NREM and REM sleep in the HPC, AMG, and ANT for the five subjects.

The mechanisms underpinning the complex temporal dynamics and sleep–wake state-dependent impedance cycles cannot be definitively determined from the data presented here. We postulate that ECS volume changes drive the ultradian and

circadian impedance cycles in human brain given the strong dependence of electrical impedance on ECS volume (Ranck, 1970; Nicholson and Hrabětová, 2017) and recent demonstration of ECS volume expansion in rodent cortex during NREM sleep

(Xie et al., 2013; Rasmussen et al., 2022). The impedance data are indirect evidence that sleep–wake state transitions (wakefulness, NREM, and REM sleep) differentially modulate human ECS and is consistent with the ECS dynamics proposed for a human brain glymphatic system (Hablitz and Nedergaard, 2021). The vascular and intracellular compartment conductances will have limited contributions to composite impedance with the current probe used here because of the high impedance of the blood–brain barrier and neuronal and glial cell membranes. The electrode–tissue interface contribution to the impedance is not expected to depend on the sleep–wake state and should not differentially contribute to impedance changes.

The interstitial-fluid-filled ECS at the known physiological volume fraction (~ 0.2) and complex cellular geometry provides a highly conductive network (Nicholson and Hrabětová, 2017) that may be near the percolation threshold enabling significant impedance changes with relatively small ECS volume changes (Bergman and Stroud, 1992; Halperin and Bergman, 2010).

We can estimate the ECS volume change, ΔV_{ECS} , that would produce the observed circadian impedance change ΔZ . The impedance change is related to the change in effective specific brain conductivity $\Delta Z = 1/4\pi a \Delta \sigma_{\text{eff}}$, where a is the cathode/anode stimulation electrode separation. The effective specific conductivity of a composite media of cells embedded in the ECS volume is $\Delta \sigma_{\text{eff}} = \frac{3}{2} \sigma_{\text{ISF}} \Delta V_{ECS}$ (Ranck, 1966; Halperin and Bergman 2010), where σ_{ISF} is the conductivity of the interstitial fluid. Using $\sigma_{\text{ISF}} \cong 1.79 \text{ S/m}$ for the conductivity of the ECS interstitial fluid (Baumann et al., 1997) and adjusting the ECS percolation threshold volume fraction to 0.07 (Halperin and Bergman 2010), a brain-specific conductivity of $\sim 0.250 \text{ S/m}$ (Ranck, 1966) yields reasonable agreement with reported ECS volume fraction of ~ 0.16 (Nicholson and Hrabětová, 2017).

In the real-time iontophoretic tetramethylammonium diffusion (Nicholson, 1993) studies in mice the ECS volume in wakefulness was 0.136 and expanded to 0.227 in the anesthetic state, a $\Delta V_{ECS} \cong 0.09$ which is a 67% relative volume change (Xie et al., 2013). In the composite conductivity model above this corresponds to a change in specific conductivity of $\Delta \sigma_{\text{eff}} = 0.24 \text{ S/m}$. A measured $\Delta Z \approx 30 \Omega$ in human AMG and HPC corresponds to a specific conductivity change of $\Delta \sigma_{\text{eff}} = 0.29 \text{ S/m}$ from wakefulness to NREM sleep and a corresponding $\Delta V_{ECS} = 0.10$. Based on this model, the human ECS volume change associated with transition to NREM sleep is slightly larger than what is observed in mice.

For these reasons, we propose that ECS volume dynamics likely underlie the observed sleep–wake state dependence and multiscale impedance cycles. A less likely, alternative hypothesis is that sleep state-dependent change in astrocyte membrane impedance combined with a gap-junction-mediated astrocytic syncytium network could provide a low impedance pathway and cannot be excluded with the current data (Ranck, 1966). Additionally, changes in ionic conductivity because of ion concentration changes in the interstitial fluid could have an effect (Ding et al., 2016). These seem less likely, and given the previous two-photon imaging and real-time iontophoretic tetramethylammonium diffusion findings in mouse cortex during NREM and anesthesia, the observed ECS volume changes would have a large effect on impedance (Xie et al., 2013).

This study has multiple limitations in understanding the physiological origin of impedance oscillations. (1) The sample size is small with only five subjects studied. It should be noted, though, the data collected are immense with continuous sampling of human intracranial brain impedance and electrophysiology over multiple months. To our knowledge similar studies

have not been previously possible. (2) The data are from people with focal epilepsy, and seizures are known to affect brain impedance (Elazar et al., 1966; Fox et al., 2004) and ECS volume (Binder et al., 2004). Despite our selection of data segments without seizures and brain electrodes with low IES rates and not involved in seizure onset there is electrophysiological evidence that the brain regions analyzed are not entirely normal. As is generally the case in limbic network epilepsy, there are IESs throughout the limbic network in all subjects (Table 1). It is also notable that the impedance fluctuations on the days with seizures, which are excluded in our analysis, show impedance differences compared with days without seizures (Figure 4). We find that seizures tend to occur at specific times of the day as previously reported in temporal epilepsy (Durazzo et al., 2008; Hofstra and de Weerd, 2009), and the impedance is higher on the days with seizures (Figure 4). We are currently investigating this phenomenon, but it suggests that epileptic brain impedance may be changed at baseline and vary with seizure risk. (3) The two-point impedance measurements introduce electrode–tissue interface effects and frequency dispersion (Fig. 2). The fact that electrical stimulation acutely decreases baseline impedance (Johnson et al., 2005) without affecting the presence or characteristics of circadian impedance cycles further supports the argument that impedance cycles are not related to changes at the electrode–tissue interface. (4) The claim that ECS dynamics underlie the impedance oscillations is not directly proven with the current data. In future we plan animal experiments not currently feasible in humans using two-photon imaging and high temporal resolution impedance sampling to investigate impedance, ECS dynamics, and the cycles of brain excitability observed in interictal epileptiform spike rates and seizures.

References

- Anastassiou CA, Perin R, Markram H, Koch C (2011) Ephaptic coupling of cortical neurons. *Nat Neurosci* 14:217–223.
- Bard AJ, Faulkner LR (2001) *Electrochemical methods: fundamentals and applications*. 2nd ed. New York: Wiley.
- Baud MO, Kleen JK, Mirro EA, Andrechak JC, King-Stephens D, Chang EF, Rao VR (2018) Multi-day rhythms modulate seizure risk in epilepsy. *Nat Commun* 9:88.
- Baumann SB, Wozny DR, Kelly SK, Meno FM (1997) The electrical conductivity of human cerebrospinal fluid at body temperature. *IEEE Trans Biomed Eng* 44:220–223.
- Bazil CW (2017) Sleep and epilepsy. *Semin Neurol* 37:407–412.
- Bergman DJ, Stroud D (1992) Physical properties of macroscopically inhomogeneous media. In: *Solid state physics* (Ehrenreich H, Turnbull D, eds), pp 147–269. Amsterdam: Academic Press.
- Berry RB, Brooks R, Gamaldo CE, Harding SM, Marcus CL, Vaughn BV (2012) *The AASM Manual for the Scoring of Sleep and Associated Events: Rules, Terminology and Technical Specifications, Version 2.0*. Darien, IL: American Academy of Sleep Medicine.
- Binder DK, Papadopoulos MC, Haggie PM, Verkman AS (2004) *In vivo* measurement of brain extracellular space diffusion by cortical surface photobleaching. *J Neurosci* 24:8049–8056.
- Butson CR, Cooper SE, Henderson JM, McIntyre CC (2007) Patient-specific analysis of the volume of tissue activated during deep brain stimulation. *Neuroimage* 34:661–670.
- Buzsáki G, Anastassiou CA, Koch C (2012) The origin of extracellular fields and currents—EEG, ECoG, LFP and spikes. *Nat Rev Neurosci* 13:407–420.
- Destrieux C, Fischl B, Dale A, Halgren E (2010) Automatic parcellation of human cortical gyri and sulci using standard anatomical nomenclature. *Neuroimage* 53:1–15.
- Ding FF, O'Donnell J, Xu QW, Kang N, Goldman N, Nedergaard M (2016) Changes in the composition of brain interstitial ions control the sleep–wake cycle. *Science* 352:550–555.

- Durazzo TS, Spencer SS, Duckrow RB, Novotny EJ, Spencer DD, Zaveri HP (2008) Temporal distributions of seizure occurrence from various epileptogenic regions. *Neurology* 70:1265–1271.
- Elazar Z, Kado RT, Adey WR (1966) Impedance changes during epileptic seizures. *Epilepsia* 7:291–307.
- Fischl B, Kowu A, Destrieux C, Halgren E, Ségonne F, Salat DH, Busa E, Seidman LJ, Goldstein J, Kennedy D, Caviness V, Makris N, Rosen B, Dale AM (2004) Automatically parcellating the human cerebral cortex. *Cereb Cortex* 14:11–22.
- Fox JE, Bikson M, Jefferys JGR (2004) Tissue resistance changes and the profile of synchronized neuronal activity during ictal events in the low-calcium model of epilepsy. *J Neurophysiol* 92:181–188.
- Gilon RA, Little S, Perrone R, Wilt R, de Hemptinne C, Yaroshinsky MS, Racine CA, Wang SS, Ostrem JL, Larson PS, Wang DD, Galifianakis NB, Bledsoe IO, San Luciano M, Dawes HE, Worrell GA, Kremen V, Borton DA, Denison T, Starr PA (2021) Long-term wireless streaming of neural recordings for circuit discovery and adaptive stimulation in individuals with Parkinson's disease. *Nat Biotechnol* 39:1078–1085.
- Gregg NM, Nasser M, Kremen V, Patterson EE, Sturges BK, Denison TJ, Brinkmann BH, Worrell GA (2020) Circadian and multiday seizure periodicities, and seizure clusters in canine epilepsy. *Brain Commun* 2:fcaa008.
- Gregg NM, Sladky V, Nejedly P, Mivalt F, Kim I, Balzekas I, Sturges BK, Crowe C, Patterson EE, Van Gompel JJ, Lundstrom BN, Leyde K, Denison TJ, Brinkmann BH, Kremen V, Worrell GA (2021) Thalamic deep brain stimulation modulates cycles of seizure risk in epilepsy. *Sci Rep* 11:24250.
- Hablitz LM, Nedergaard M (2021) The glymphatic system: a novel component of fundamental neurobiology. *J Neurosci* 41:7698–7711.
- Halperin BI, Bergman DJ (2010) Heterogeneity and disorder: contributions of Rolf Landauer. *Physica B Condens Matter* 405:2908–2914.
- Hermes D, Miller KJ, Noordmans HJ, Vansteensel MJ, Ramsey NF (2010) Automated electrocorticographic electrode localization on individually rendered brain surfaces. *J Neurosci Methods* 185:293–298.
- Hofstra WA, de Weerd W (2009) The circadian rhythm and its interaction with human epilepsy: a review of literature. *Sleep Med Rev* 13:413–420.
- Holth JK, Fritsch SK, Wang C, Pedersen NP, Cirrito JR, Mahan TE, Finn MB, Manis M, Geerling JC, Fuller PM, Lucey BP, Holtzman DM (2019) The sleep-wake cycle regulates brain interstitial fluid tau in mice and CSF tau in humans. *Science* 363:880–884.
- Horn A, Li N, Dembek TA, Kappel A, Boulay C, Ewert S, Tietze A, Husch A, Perera T, Neumann WJ, Reiser M, Si H, Oostenveld R, Rorden C, Yeh FC, Fang Q, Herrington TM, Vorwerk J, Kühn AA (2019) Lead-DBS v2: towards a comprehensive pipeline for deep brain stimulation imaging. *Neuroimage* 184:293–316.
- Janca R, et al. (2014) Detection of Interictal Epileptiform Discharges Using Signal Envelope Distribution Modelling: Application to Epileptic and Non-Epileptic Intracranial Recordings. *Brain Topography* 28:172–183.
- Jefferys JGR, Prida L, Wendling F, Bragin A, Avoli M, Timofeev I, Lopes da Silva FH (2012) Mechanisms of physiological and epileptic HFO generation. *Prog Neurobiol* 98:250–264.
- Johnson MD, Otto KJ, Kipke DR (2005) Repeated voltage biasing improves unit recordings by reducing resistive tissue impedances. *IEEE Trans Neural Syst Rehabil Eng* 13:160–165.
- Karoly PJ, Rao VR, Gregg NM, Worrell GA, Bernard C, Cook MJ, Baud MO (2021) Cycles in epilepsy. *Nat Rev Neurol* 17:267–284.
- Koessler L, Colnat-Coulbois S, Cecchin T, Hofmanis J, Dmochowski JP, Norcia AM, Maillard LG (2017) *In-vivo* measurements of human brain tissue conductivity using focal electrical current injection through intracerebral multicontact electrodes. *Hum Brain Mapp* 38:974–986.
- Kremen V, et al. (2018) Integrating brain implants with local and distributed computing devices: a next generation epilepsy management system. *IEEE J Transl Eng Health Med* 6:2500112.
- Kremen V, et al. (2017) Behavioral State Classification in Epileptic Brain Using Intracranial Electrophysiology. *J Neural Eng* 14:026001.
- Kremen V, Brinkmann BH, Gompel JJV, Stead M, Louis EKS, Worrell GA (2019) Automated unsupervised behavioral state classification using intracranial electrophysiology. *J Neural Eng* 16:026004.
- Kuiper NH (1960) Tests concerning random points on a circle. *Indagationes Mathematicae (Proceedings)* 63:38–47.
- Larson R, Odoni A (1981) Urban operations research. Englewood Cliffs, NJ: Prentice Hall.
- Lempka SF, Miocinovic S, Johnson MD, Vitek JL, McIntyre CC (2009) *In vivo* impedance spectroscopy of deep brain stimulation electrodes. *J Neural Eng* 6:046001.
- Logothetis NK, Kayser C, Oeltermann A (2007) *In vivo* measurement of cortical impedance spectrum in monkeys: implications for signal propagation. *Neuron* 55:809–823.
- Miceli S, Ness TV, Einevoll GT, Schubert D (2017) Impedance spectrum in cortical tissue: implications for propagation of LFP signals on the microscopic level. *eNeuro* 4:ENEURO.0291-16.2016.
- Mivalt F, Kremen V, Sladky V, Balzekas I, Nejedly P, Gregg NM, Lundstrom BN, Lepkova K, Pridalova T, Brinkmann BH, Jurak P, Gompel JJV, Miller K, Denison T, Louis EKS, Worrell GA (2022) Electrical brain stimulation and continuous behavioral state tracking in ambulatory humans. *J Neural Eng* 19:016019.
- Nicholson C (1993) Ion-selective microelectrodes and diffusion measurements as tools to explore the brain-cell microenvironment. *J Neurosci Methods* 48:199–213.
- Nicholson C, Hrabětová S (2017) Brain extracellular space: the final frontier of neuroscience. *Biophys J* 113:2133–2142.
- Pal Attia T, Crepeau D, Kremen V, Nasser M, Guragain H, Steele SW, Sladky V, Nejedly P, Mivalt F, Herron JA, Stead M, Denison T, Worrell GA, Brinkmann BH (2021) Epilepsy personal assistant device, a mobile platform for brain state, dense behavioral and physiology tracking and controlling adaptive stimulation. *Front Neurol* 12:704170.
- Penny WD, Friston KJ, Ashburner JT, Kiebel SJ, Nichols TE (2011) Statistical parametric mapping: the analysis of functional brain images. Amsterdam: Elsevier.
- Percival DB, Walden AT (1993) Spectral analysis for physical applications. Cambridge, UK: Cambridge UP.
- Qiu C, Shivacharan RS, Zhang M, Durand DM (2015) Can neural activity propagate by endogenous electrical field? *J Neurosci* 35:15800–15811.
- Ranck JB (1966) Electrical impedance in the subicular area of rats during paradoxical sleep. *Exp Neurol* 16:416–437.
- Ranck JB (1970) Electrical impedance changes in many sites of brain in paradoxical sleep, anesthesia, and activity. *Exp Neurol* 27:454–475.
- Rasmussen MK, Mestre H, Nedergaard M (2022) Fluid transport in the brain. *Physiol Rev* 102:1025–1151.
- Sauerheber R, Heinz B (2015) Temperature effects on conductivity of seawater and physiologic saline, mechanism and significance. *Chem Sci* 6:56087588.
- Savtchenko LP, Poo MM, Rusakov DA (2017) Electrodiffusion phenomena in neuroscience: a neglected companion. *Nat Rev Neurosci* 18:598–612.
- Savtchenko LP, Zheng K, Rusakov DA (2021) Conductance of porous media depends on external electric fields. *Biophys J* 120:1431–1442.
- Sillay KA, Rutecki P, Cicora K, Worrell G, Drakowski J, Shih JJ, Sharan AD, Morrell MJ, Williams J, Wingeier B (2013) Long-term measurement of impedance in chronically implanted depth and subdural electrodes during responsive neurostimulation in humans. *Brain Stimul* 6:718–726.
- Sladky V, et al. (2022) Distributed brain co-processor for tracking spikes, seizures and behaviour during electrical brain stimulation. *Brain Commun* 4:fcaa115.
- Stanslaski S, Herron J, Chouinard T, Bourget D, Isaacson B, Kremen V, Opri E, Drew W, Brinkmann BH, Gunduz A, Adamski T, Worrell GA, Denison T (2018) A chronically implantable neural coprocessor for investigating the treatment of neurological disorders. *IEEE Trans Biomed Circuits Syst* 12:1230–1245.
- Thomson DJ (1982) Spectrum estimation and harmonic analysis. *Proc IEEE* 70:1055–1096.
- Xie L, Kang H, Xu Q, Chen MJ, Liao Y, Thiyagarajan M, O'Donnell J, Christensen DJ, Nicholson C, Iliff JJ, Takano T, Deane R, Nedergaard M (2013) Sleep drives metabolite clearance from the adult brain. *Science* 342:373–377.